Microstructure and Properties of Laser Brazed Magnesium to Coated Steel

The aluminum coating on the steel sheet was found to be a key factor for facilitating laser brazing of the Mg alloy to the sheet

BY A. M. NASIRI, L. LI, S. H. KIM, Y. ZHOU, D. C. WECKMAN, AND T. C. NGUYEN

ABSTRACT

A diode laser brazing procedure has been developed for joining AZ31B-H24 Mg alloy sheet to aluminum-coated, cold-rolled carbon steel sheet in the single flare bevel lap joint configuration using a Mg-Al based welding wire. In this process, the Mg-Al based filler metal and a shallow surface layer of the Mg alloy sheet were melted simultaneously by a diode laser beam, while no melting of the steel sheet occurred. The results of this study suggest that feasibility of this process depends strongly on the preexisting Al-12Si coating layer on the steel sheet that promotes wetting of the Mg-Al filler alloy as well as formation of a layer of θ-Fe(Al,Si)$_3$ intermetallic compound along the braze/steel interface. From the middle part of the braze/steel interface to the root of the joint, the Al-Si layer melted and mixed into the braze alloy and the intermetallic layer grew up to 8 μm thick. From the middle part of the braze/steel interface to the top of the joint, both the Al-Si and the intermetallic layer were dissolved. These two simultaneous phenomena led to an intermetallic layer with nonuniform thickness ranging from 0 to 8 μm along the braze/steel interface. The average fracture load of the joint was 767 N, representing a 72% joint efficiency relative to the steel sheet. Failure occurred when cracks propagated along the intermetallic layer starting at the root of the bevel joint and moved into the braze metal at the upper part of the joint.

Introduction

In recent years, interest has grown in the joining of dissimilar metal combinations. In the automotive and aerospace industries (Refs. 1, 2), the development of dissimilar metal joints is a natural advancement of the concept of tailor-welded blanks (TWBs). Besides allowing further improvements and optimization of material utilization and mechanical properties in parts, dissimilar metal joints can offer additional benefits related to functionality requirements (Ref. 3). To date, researchers have focused on joining of dissimilar metals such as aluminum to steel and aluminum to titanium, using solid-state (Refs. 4, 5), reactive wetting (Refs. 6–8), and laser welding (Refs. 9, 10) joining processes.

The use of high strength-to-weight ratio magnesium alloys in automotive structures is attractive because it can help to lower the overall weight of the vehicle, thereby facilitating improvement in fuel efficiency and reduction of harmful greenhouse gas emissions (Ref. 11). The increased application of Mg alloys in automotive structures will be further facilitated by research and development of methods for joining steel to Mg alloys. To date, only limited studies have been conducted in the joining of magnesium alloys to steel. Friction stir welding (FSW) (Ref. 12) and laser-arc hybrid welding (Refs. 13–16) techniques to join magnesium alloys to steel have been examined.

Solid-state joining processes, such as FSW, can be used to make dissimilar metal joints between Mg and steel (Refs. 12, 17). However, the designs of FSW joints are restricted. Also, FSW is difficult to use as a joining process in industry, especially for high-melting-point materials like steel, because heavy-duty clamping systems are required to hold the parts together and also there are difficulties with thickness variation and nonlinear welds. Joint strengths up to 70% of the Mg base material strength have been obtained when using the FSW process to join Mg alloys to steel (Ref. 12).

Fusion welding processes are normally not suitable for joining of Mg and steel due to the large difference in melting temperatures between Mg and steel, i.e., 649° and 1538°C, respectively. In addition, the boiling point of magnesium is only 1091°C. As a result, molten steel will vaporize magnesium that is in contact with it. At ambient pressure, molten magnesium and molten steel do not mix nor react with each other (Ref. 18). Catastrophic vaporization of the magnesium is inevitable when using recently developed fusion welding processes such as laser-gas tungsten arc hybrid welding. In addition, protection of the steel-Mg alloy interface from oxidation in a lap joint design is difficult (Refs. 13–16).

The benefits of using laser brazing and laser welding-brazing technologies for joining dissimilar materials are becoming increasingly recognized due to the combined attributes of furnace brazing and laser welding (Ref. 19). With a more localized energy input and more precise

A. M. NASIRI (amnasiri@uwaterloo.ca), *L. LI, S. H. KIM, Y. ZHOU, and D. C. WECKMAN are with Department of Mechanical & Mechatronics Engineering, Center for Advanced Materials Joining, University of Waterloo, Waterloo, Ont., Canada. T. C. NGUYEN is with School of Engineering and Information Technology, Conestoga College, Kitchener, Ont., Canada. LI is also with State Key Laboratory of Advanced Welding Production and Technology, Harbin Institute of Technology, Harbin, China. KIM is also with Welding Research Center, Research Institute of Industrial Science & Technology, Hyoja-Dong, Nam-Ku, Pohang City, Korea.*

KEYWORDS

Laser Brazing
AZ31B Mg Sheet
Aluminum Coated Steel Sheet
Intermetallic Compound

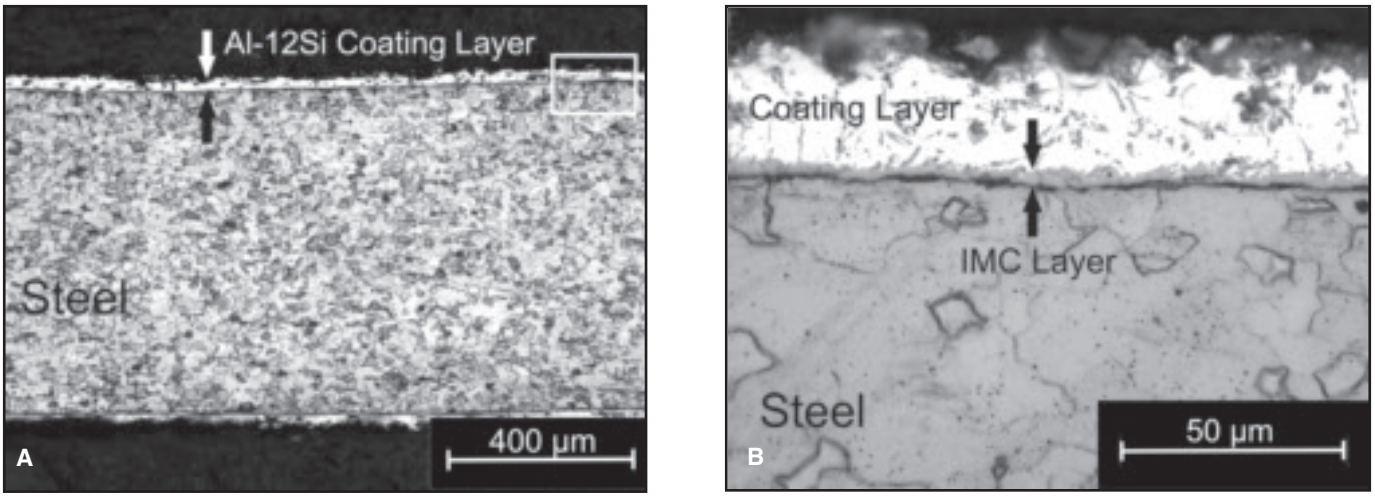

Fig. 1 — Transverse section of original steel sheet showing: A — The Al-12Si coating layer; B — the preexisting Fe-Al-Si IMC layer at the steel/coating layer interface.

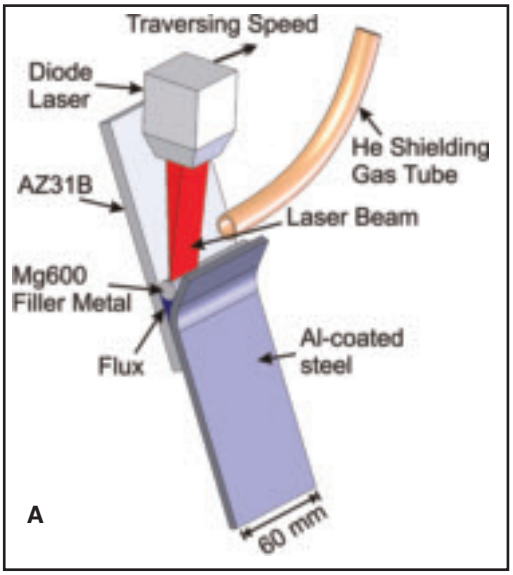

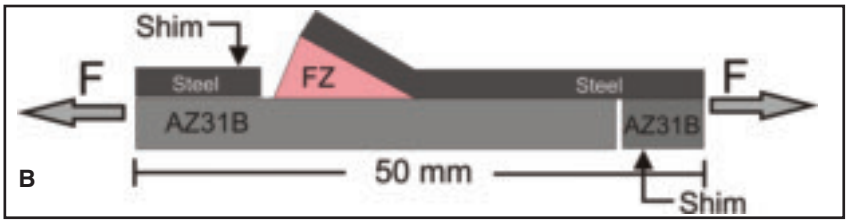

Fig. 2 — A — Schematic of the laser brazing system used for joining the AZ31 Mg and aluminum-coated steel sheets in the single flare bevel lap joint configuration; B — schematic of the 5-mm-wide tensile shear test specimens.

Table 1 — Measured Chemical Compositions of the AZ31-H24 Mg Alloy Sheet and TiBraze Mg 600 Filler Metal (wt-%)

	Al	Zn	Mn	Si	Mg
AZ31B-H24	3.02	0.80	0.30	0.01	Bal.
TiBraze Mg 600	9	2	0.2	—	Bal.

control of the laser beam energy, high joining speeds and accompanying high cooling rates can be realized with minimal heating of the parts. Also, laser brazing and laser welding-brazing can prevent or minimize excessive formation of detrimental intermetallic phases. The formation of intermetallic layers can be limited to a size below 10 μm, which leads to desirable mechanical properties (Refs. 3, 19, 20). Miao et al. (Refs. 21, 22) developed the technology for laser penetration brazing (LPB) of a magnesium alloy to steel using a high-power CO_2 laser without welding wire. In this process, the laser beam was radiated on the magnesium alloy side of a butt joint to get full fusion of the magnesium alloy (Ref. 21). However, melting of the steel side was inevitable, and cracking and porosity occurred at the interface due to evaporation of magnesium and lack of solubility and reaction between the magnesium alloy and the steel (Ref. 21). A direct relationship was found between weld cracking and excessive melting of the steel (Ref. 21).

A lower-intensity laser beam, such as provided by a diode laser, can be used with welding wire to control the heat flow in a laser brazing process, thus avoiding melting of the steel. In such a process, the welding wire and surface of the Mg alloy base material are melted simultaneously by a high-power diode laser, while the steel remains unmelted. In the present study, a procedure has been developed for laser brazing of AZ31B-H24 magnesium alloy to aluminum-coated steel sheet. The brazing process was designed to avoid the vaporization of magnesium. The aim of this work was to investigate the microstructure and mechanical properties of the brazed joints between the Mg alloy and Al-12Si coated steel sheet using a welding wire.

Experimental Procedures

In the present study, 2-mm-thick commercial grade twin-roll strip cast AZ31B-H24 Mg alloy sheet and 1-mm-thick aluminum-coated steel sheet were used. The Al-12 wt-% Si coating layer on the steel sheet was 20 ± 2 μm thick. The AZ31B Mg sheet contained Mn for improved corrosion resistance (Ref. 23). The compositions of these materials are given in Tables 1 and 2. An optical microscopic image of the steel/Al-12Si coating layer interface before the brazing process is shown in Fig. 1. In Fig. 1B, a 3.5-μm-thick Fe-Al-Si intermetallic compound (IMC) layer is clearly shown at the interface. This IMC layer was confirmed by X-ray diffraction to be the θ-$Fe(Al,Si)_3$ phase.

A 2.4-mm-diameter TiBraze Mg 600 welding wire with solidus and liquidus temperatures of 445° and 600°C, respectively, was chosen for this study. The composition of the filler metal is shown in Table 1. This brazing alloy is compatible with the AZ31B magnesium base metal alloy. The commercial flux used in the experiments was Superior No. 21 manufactured by Superior Flux and Mfg. Co. This

Table 2 — Measured Chemical Composition of the Aluminum-Coated Steel Sheet (wt-%)

C	Mn	P	S	Fe
0.004	0.6	0.010	0.004	Bal.

powder flux was composed of LiCl (35–40 wt-%), KCl (30–35 wt-%), NaF (10–25 wt-%), NaCl (8–13 wt-%), and $ZnCl_2$ (6–10 wt-%) (Ref. 24).

The AZ31 Mg and steel sheets were cut into 60 × 50 mm specimens. Prior to brazing, the oxide layers on the surface of the magnesium sheets were removed by stainless steel wire brushing. All the specimens were ultrasonically cleaned in acetone to remove oil and other contaminants from the specimen surfaces.

A diagram of the laser brazing apparatus used is shown in Fig. 2A. The edge of the steel sheet was bent and clamped against the magnesium sheet to make a single flare bevel lap joint. The welding wire was cut into pieces and preset on the workpiece at the fusion zone with some flux before heating and brazing by the laser beam.

A Nuvonyx diode laser system with a maximum power of 4.0 kW and a Panasonic six-axis robot were used in this work. The intensity distribution of the laser beam at the focal point was rectangular in shape (1 × 12 mm) with a uniform intensity profile. This uniform energy distribution is more suitable for brazing processes compared with the nonuniform Gaussian-distributed circular beams generated by CO_2 and Nd:YAG lasers (Ref. 25). The beam was focused on top of the filler metal.

In order to limit oxidation, helium shielding gas was provided in front of the molten pool with a flow rate of 30 L/min from a 6-mm-diameter soft copper feeding tube. The process parameters were 1.8 to 2.4 kW laser power, 5 to 10 mm/s travel speed, and –0.2 to 0.4 mm beam position offset relative to the steel.

After laser brazing, typical transverse cross-sections of the brazed specimens were cut and mounted in epoxy resin. The samples were then mechanically polished using 300, 600, 800, and 1000 grades of SiC grinding papers followed by polishing using a 1-μm diamond suspension. The polished specimens were etched to reveal the microstructure of the braze metal and AZ31B base material. The etchant was comprised of 20mL acetic acid, 3-g picric acid, 50mL ethanol, and 20mL water (Ref. 26). Macro- and microstructures of the joints were observed using an optical metallographic microscope. The microstructure and composition of different zones at the joint cross section were determined using a JEOL JSM-6460 scanning electron microscope (SEM) and energy-dispersive X-ray spectrometer (EDS). Phase characterization of the steel fusion zone and the steel/Al-12Si coating layer interfaces after laser brazing was determined using X-ray diffraction (XRD) phase analysis with a Cu K_α source.

Vickers microhardness profiles across the brazed joints were measured using a 50-g loading force and 10-s holding time. As shown in Fig. 2B, the brazed 5-mm-wide, rectangular-shaped specimens were cut and subjected to tensile shear tests with a crosshead speed of 1 mm/min. Shims were used at each end of the specimens to ensure shear loads in the lap joint while minimizing induced couples or bending of the specimens. Average tensile shear strength was calculated from tensile specimens to estimate the static mechanical resistance of the joints.

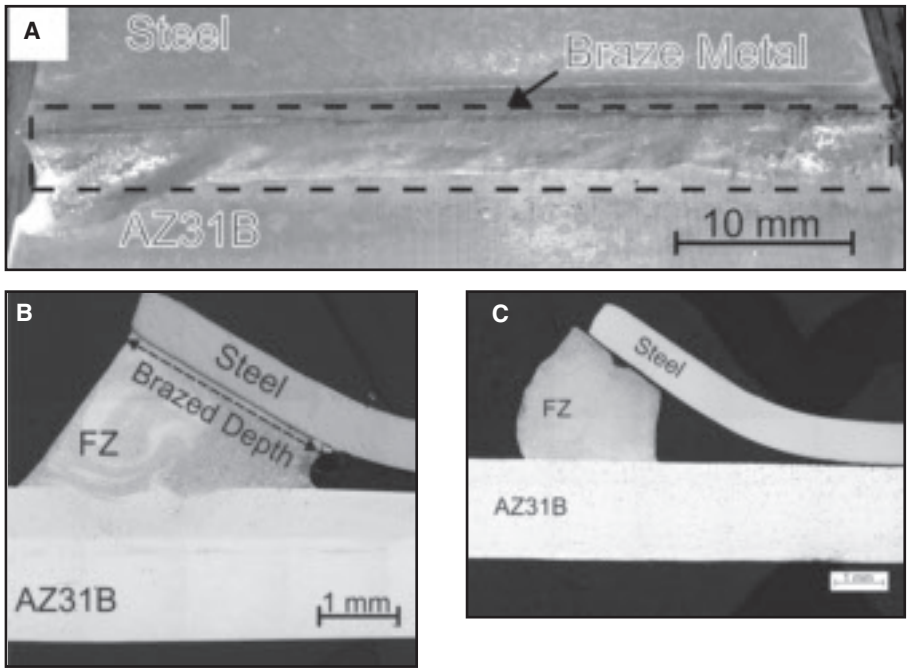

Fig. 3 — Laser brazed AZ31B-to-steel sheets made using 8 mm/s travel speed and 2.2 kW laser beam power: A — Top bead; B — transverse section of a brazed Al-12Si coating steel; C — transverse section of a brazed uncoated steel sheet.

Table 3 — EDS Analysis Results of IMC Layers at the Original Steel/Coating Layer Interface Shown in Fig. 7 (wt-%)

IMC	Al	Si	Fe
I (P1–P4)	56.6 ± 1.4	10.4 ± 0.1	32.9 ± 1.3
II (P5–P8)	62.6 ± 2.6	16.1 ± 1.6	21.3 ± 1.2

Results and Discussion

Microstructures of the Brazed Joints

The top surface appearance of a laser brazed joint and typical cross-sectional views of laser brazed Mg to steel are shown in Fig. 3. When using 2.2-kW laser power, 8-mm/s travel speed, and 0.2-mm beam offset to the steel side, a uniform brazed area with good wetting of both base materials and some partial melting of the AZ31B base metal was observed. In contrast, using bare steel resulted in no bonding between steel and the braze alloy fusion zone (FZ) and the wetting of the steel by the braze metal was very poor (see Fig. 3C). The Al-Si coating on the surface of the steel significantly improved the wetting of the steel by molten Mg-Al filler metal resulting in metallurgical bonding with the fusion zone.

The typical microstructure of a laser brazed AZ31B/steel joint transverse section and higher-magnification images of various locations are shown in Fig. 4. Grain growth toward the fusion boundary occurred in the AZ31B heat-affected zone (HAZ), as shown in Fig. 4B.

In the partially melted zone (PMZ), localized melting or liquation of intergranular regions occurred as indicated in Fig. 4C. The thickness of the PMZ layer was

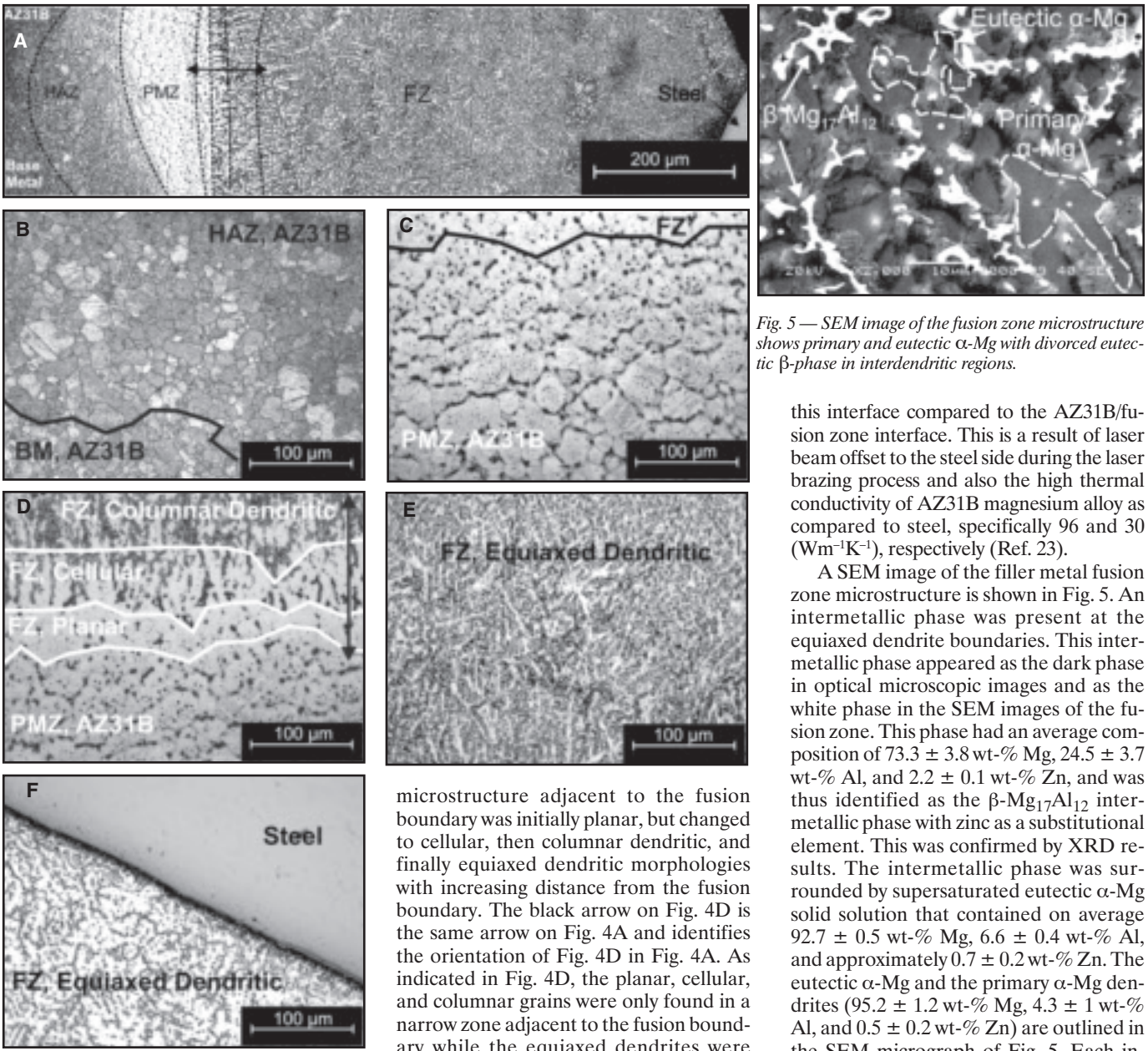

Fig. 4 — Photomicrographs of different microstructural regions in the laser brazed AZ31B/steel joint.

not uniform around the fusion zone (20–100 μm) due to the temperature gradient resulting from the laser brazing process. Inspection by optical microscopy suggested that the small extent of the liquated region did not result in intergranular cracking upon cooling.

As shown in Fig. 4D, the solidification microstructure adjacent to the fusion boundary was initially planar, but changed to cellular, then columnar dendritic, and finally equiaxed dendritic morphologies with increasing distance from the fusion boundary. The black arrow on Fig. 4D is the same arrow on Fig. 4A and identifies the orientation of Fig. 4D in Fig. 4A. As indicated in Fig. 4D, the planar, cellular, and columnar grains were only found in a narrow zone adjacent to the fusion boundary while the equiaxed dendrites were dominant in the fusion zone. The microstructure in the center of the fusion zone was homogeneous and characterized by numerous equiaxed dendrites with fine precipitates dispersed in the interdendritic regions, as shown in Fig. 4E.

Figure 4F shows the microstructure of the fusion zone adjacent to the steel side, which was mainly equiaxed dendritic. Planar and cellular structures were not observed at this interface due to low-temperature gradient and cooling rate in this interface compared to the AZ31B/fusion zone interface. This is a result of laser beam offset to the steel side during the laser brazing process and also the high thermal conductivity of AZ31B magnesium alloy as compared to steel, specifically 96 and 30 ($Wm^{-1}K^{-1}$), respectively (Ref. 23).

Table 4 — EDS Analysis Results of the Fusion Zone at the Middle Part and at the Steel/Coating Layer Interface (wt-%)

Location	Mg	Al	Fe	Zn
R1 (near the interface)	79.5	15.7	1.9	2.9
R2 (middle part)	86.1	11.4	—	2.5

Fig. 5 — SEM image of the fusion zone microstructure shows primary and eutectic α-Mg with divorced eutectic β-phase in interdendritic regions.

A SEM image of the filler metal fusion zone microstructure is shown in Fig. 5. An intermetallic phase was present at the equiaxed dendrite boundaries. This intermetallic phase appeared as the dark phase in optical microscopic images and as the white phase in the SEM images of the fusion zone. This phase had an average composition of 73.3 ± 3.8 wt-% Mg, 24.5 ± 3.7 wt-% Al, and 2.2 ± 0.1 wt-% Zn, and was thus identified as the β-$Mg_{17}Al_{12}$ intermetallic phase with zinc as a substitutional element. This was confirmed by XRD results. The intermetallic phase was surrounded by supersaturated eutectic α-Mg solid solution that contained on average 92.7 ± 0.5 wt-% Mg, 6.6 ± 0.4 wt-% Al, and approximately 0.7 ± 0.2 wt-% Zn. The eutectic α-Mg and the primary α-Mg dendrites (95.2 ± 1.2 wt-% Mg, 4.3 ± 1 wt-% Al, and 0.5 ± 0.2 wt-% Zn) are outlined in the SEM micrograph of Fig. 5. Each interdendritic region consisted of a single β-$Mg_{17}Al_{12}$ particle surrounded by eutectic supersaturated α-Mg grown from primary α-Mg dendrites. This type of eutectic is called a divorced eutectic, since the two eutectic phases (α-Mg and β-$Mg_{17}Al_{12}$) are completely separated. This divorced eutectic morphology has previously been reported in microstructures of Mg cast alloys either with high content of zinc or high cooling rates during solidification (Refs. 27, 28). In this study, the high cooling rate of the laser brazing process and also 2 wt-% Zn content of filler metal promoted formation of divorced eutectic shown in Fig. 5.

Thermal Effect on IMC at Steel/Al-12Si Coating Interface

In order to see the thermal effect of the laser brazing process on the IMC layer on

the steel, the opposite steel surface that did not come into contact with the brazing filler metal was examined (see Fig. 6A). As shown in Fig. 6B–D, growth of the IMC layer at the interface of the steel/coating layer occurred due to high temperature experienced during the brazing process. At the upper part of the interface (Fig. 6B), the IMC layer showed two morphologies. The first morphology labeled as IMC I in Fig. 6 adjacent to the steel was a compact plate-like phase thicker than the original IMC layer. The second morphology labeled as IMC II in Fig. 6 shows long needle-like crystals, which grew from IMC I.

It was observed that upon moving from the location of Fig. 6B to the location of Fig. 6D, the needle-like crystals of IMC II gradually disappeared due to the lower temperature experienced during the process. Also, the average thickness of the IMC I layer changed significantly from 8 μm at the upper location to about 4 μm at the location of Fig. 6D compared to the original preexisting IMC layer between the coating layer and the steel, which had an average thickness of 3.5 μm.

Figure 7 shows an SEM image and XRD result of the IMC layer between the steel and Al-12Si coating near the top of the joint. EDS analysis was carried out for the IMC I layer at locations P1 to P4 in Fig. 7A, and for IMC II at locations P5 to P8. The EDS results are summarized in Table 3. According to the XRD profile of the interface in Fig. 7B and also composition of the IMCs in Table 3, the IMCs were determined to be mixtures of the θ-$Fe(Al,Si)_3$ and τ_5-$Al_{7.2}Fe_{1.8}Si$ phases. From the Fe-Al-Si ternary alloy phase diagram and typical characteristics of Fe-Al-Si systems (Refs. 29–32), the IMC I layer was determined to consist of the θ-$Fe(Al,Si)_3$ phase, and the needle-like IMC II layer was τ_5-$Al_{7.2}Fe_{1.8}Si$. These layers dissolved 10.4 and 16.1 wt-% of Si in solid solution, respectively, and Si atoms substituted for Al atoms in the IMC phases.

The rationale for having 12 wt-% Si in the composition of the coating layer is explained as follows. According to previous work on hot dip aluminizing (Ref. 33), the solubility of Fe in an aluminum bath increases from 5.3 to 12 wt-% with the content of Si increasing from 0 to 10 wt-% at 800°C. With the Al-12Si coating layer on the steel in this study, more Fe atoms were able to dissolve into the coating layer to form a thicker Fe-Al IMC layer. According to recent studies (Refs. 31, 32), the solubility of Si in Al-Fe IMC phase is 0.8–6 wt-% as substitute atoms in the θ-$FeAl_3$ phase. When up to 10 wt-% of Si atoms participate in the intermetallic phase formation, more Si atoms can dissolve in the θ-$FeAl_3$ phase to form a supersaturated solid solution during rapid cooling (Ref. 32), but this does not change the brittleness of this compound. According to Peyre et al. (Ref. 8), the same values of hardness were obtained for pure Fe-Al IMC and Fe-Al IMC containing up to 8 at-% Si (1200 ± 100 $HV20_{mN}$).

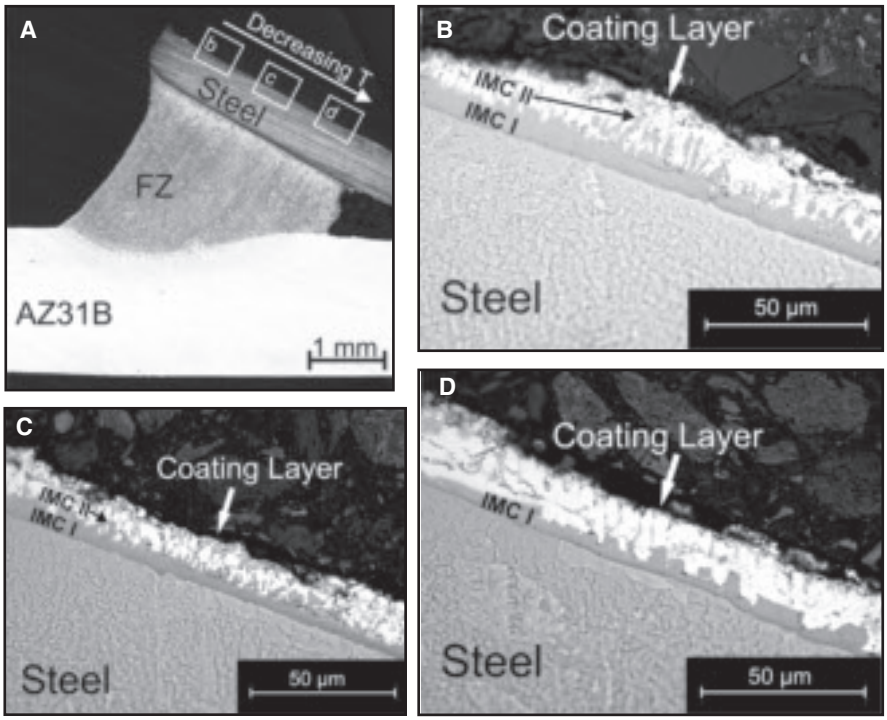

Fig. 6 — Thickness and morphology variation of IMC layer in different positions of the steel/coating layer interface indicated in the following: A, B — Upper; C — middle; D — bottom part of the joint.

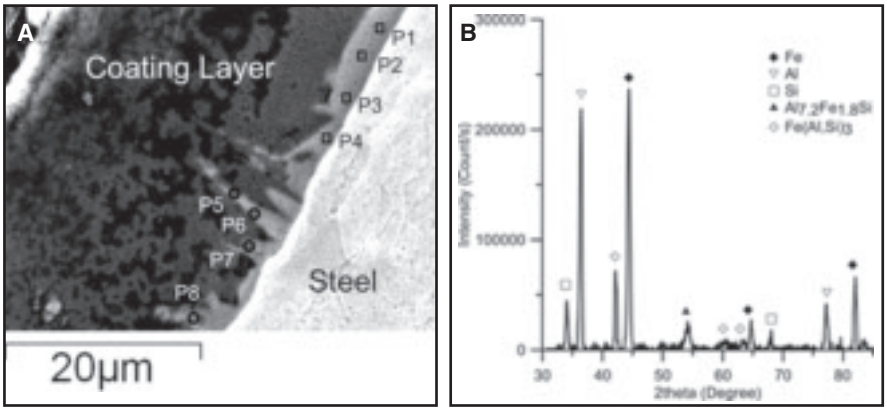

Fig. 7 — Al-12Si coating layer-steel interface of a laser brazed AZ31B-steel joint: A — SEM image of IMC layer along interface demonstrates locations with EDS analysis; B — X-ray diffraction pattern of the interface.

Table 5 — EDS Analysis Results at Different Locations on the Fracture Surface Shown in Figs. 13A and 14A (wt-%)

Element	Fusion Zone Side			Steel Side		
	Top (B)	Middle (C)	Bottom (D)	Top (F)	Middle (G)	Bottom (H)
Mg, Ka	90.18	68.88	18.05	90.01	32.69	—
Al, Ka	9.82	21.00	59.96	9.99	29.57	20.98
Fe, Ka	—	10.12	21.98	—	37.74	79.02

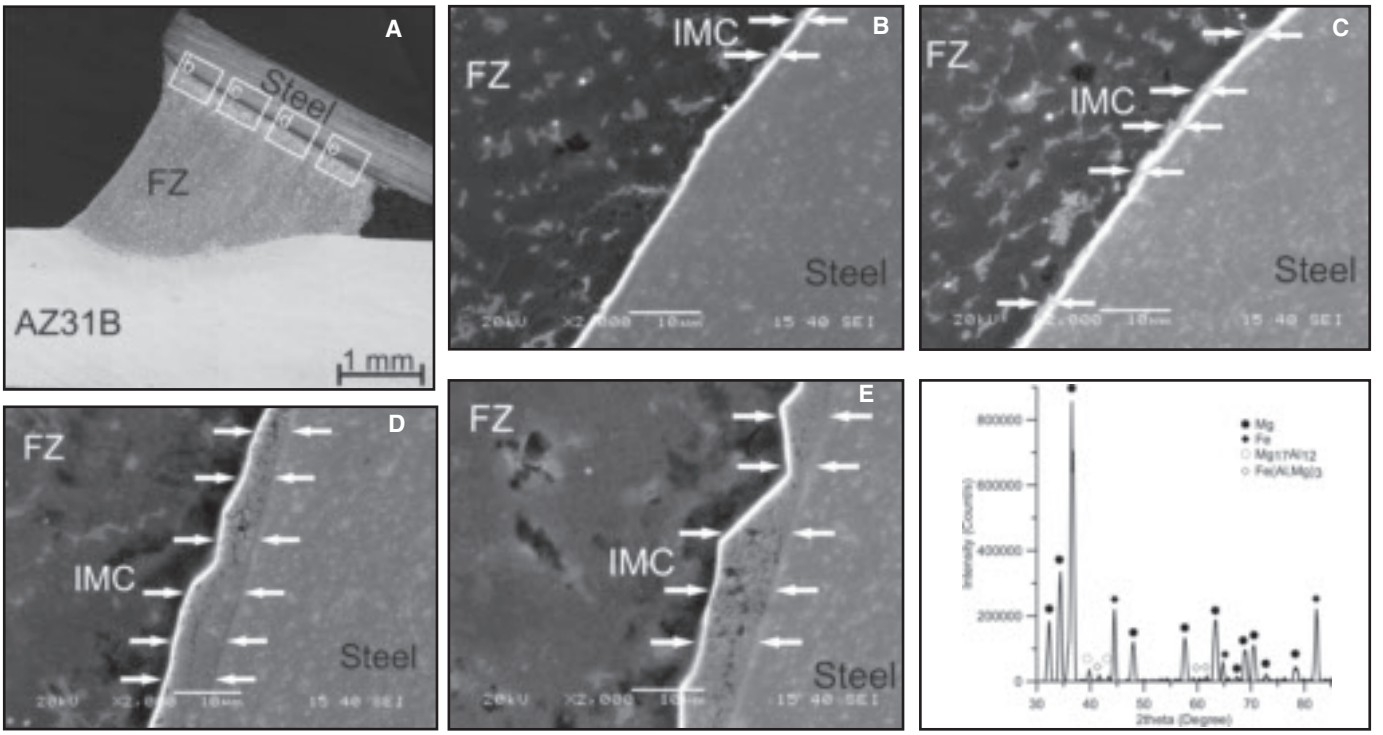

Fig. 8 — A — SEM images in different positions of the steel/FZ interface; B–E — IMC layer in b–e zones shown in A.

Fig. 9 — X-ray diffraction pattern of the steel-fusion zone interface of a laser brazed AZ31B-steel joint.

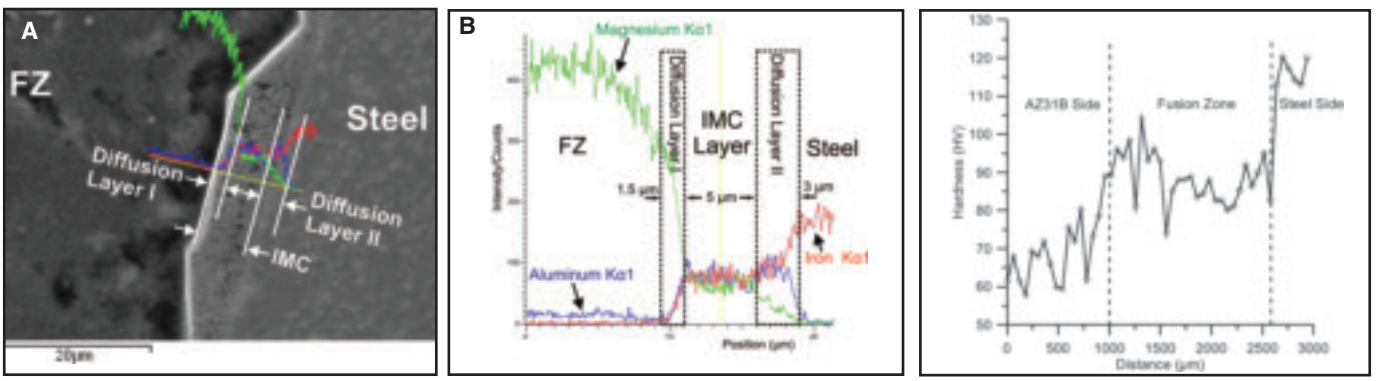

Fig. 10 — EDS composition line scans at the FZ/steel interface: A — SEM image of the interface; B — line scans of Al, Fe, and Mg.

Fig. 11 — Microhardness profile of a laser brazed AZ31B-steel joint.

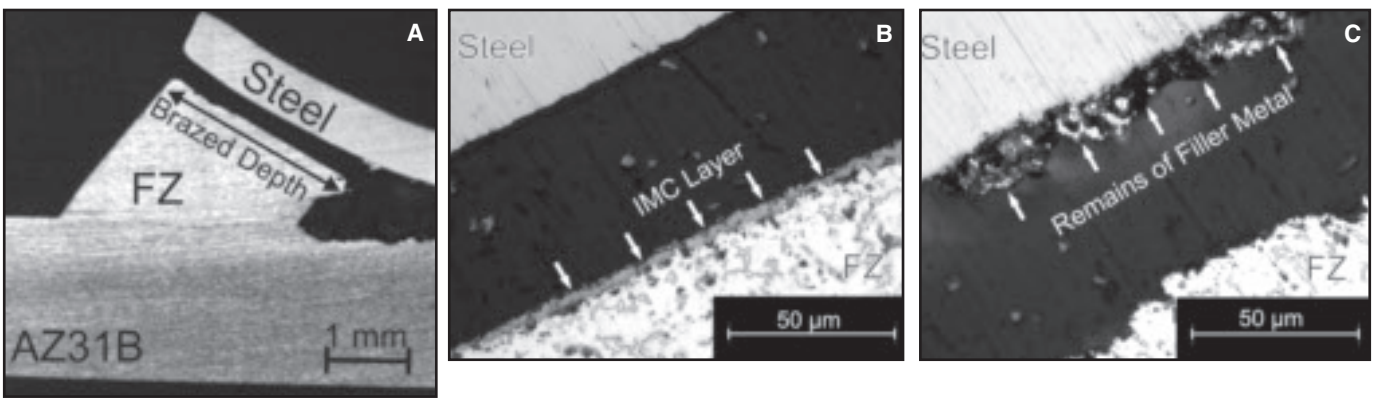

Fig. 12 — Fracture location of the tensile shear test specimen. A — Fractured specimen; B — crack propagation in bottom of the joint; C — crack propagation in upper part of the joint.

The IMC at the Steel/Fusion Zone Interface

In the laser brazing process, most of the Al-Si coating was melted and diffused into the FZ leaving only an IMC layer of nonuniform thickness as seen at the steel/braze interface in Fig. 8. Based on EDS analysis results, this IMC layer was found to contain 54.7 ± 6.1 wt-% Al, 40.1 ± 7.7 wt-% Fe, and 5.2 ± 3.7 wt-% Mg. Based on these measurements and an

XRD profile of the steel-fusion zone interface shown in Fig. 9, the IMC was identified as predominantly θ-$FeAl_3$ with some Mg diffused into the IMC layer during laser brazing.

As shown in Fig. 8, the thickness of the IMC layer at the FZ/steel interface varied along the interface. At the top, closest to the heat source of the laser, the IMC layer largely dissolved into the FZ leaving a very thin layer less than 2 μm (Fig. 8B, C). However, farther down and away from the heat of the laser beam, the IMC had grown to approximately 8 μm in thickness (see Fig. 8D). The change in the thickness of the intermetallic layers is controlled by two simultaneous phenomena: the diffusion-controlled growth of intermetallic layers and their dissolution by molten alloy (Refs. 34, 35). Roulin et al. (Ref. 36) studied the furnace brazing of steel-Al alloy dissimilar joints with Al-12Si filler metal. It was reported that the first formed phase along the steel-Al interface at 600°C was a ternary Fe-Al-Si IMC with a parabolic growth rate indicating a diffusion-controlled mechanism. At this temperature, dissolution of the IMC was negligible (Ref. 36). In contrast, Viala et al. (Ref. 35) reported the formation of a Fe-Al-Si IMC at 780°C during hot dipping of steel in molten Al-7Si alloy. It was reported that this IMC remained very thin (2–3 μm) at 780°C due to its rapid dissolution (Ref. 35). It can be concluded that with increasing temperature, the dissolution rate of Fe-Al-Si IMC increases more rapidly than the growth rate (diffusion rate).

From this information, the following mechanism can be proposed for change in IMC thickness along the steel-fusion zone interface from top to bottom portion of the joint. According to the binary phase diagram of Al-Si, the melting temperature of the eutectic composition coating layer (Al-12 wt-% Si) is approximately 577°C. When compared to the brazing temperature of the filler metal used in this study (600°~620°C), the Al-Si coating layer experienced temperatures higher than its melting point during the process. Consequently, the high temperature of the process led to the melting of the Al-Si coating and also promoted dissolution of the preexisting IMC layer between the Al-12Si coating and the steel. At the top side of the interface, the dissolution mechanism of preexisting IMC was more dominant than the diffusion growth mechanism due to the rapid temperature increase. However, with decreasing temperatures from the top toward the bottom of the interface, the IMC dissolution rate in the fusion zone decreased and its growth rate increased (decreasing temperature favors the diffusion-controlled growth mechanism more than the dissolution mechanism).

Representative concentration profiles

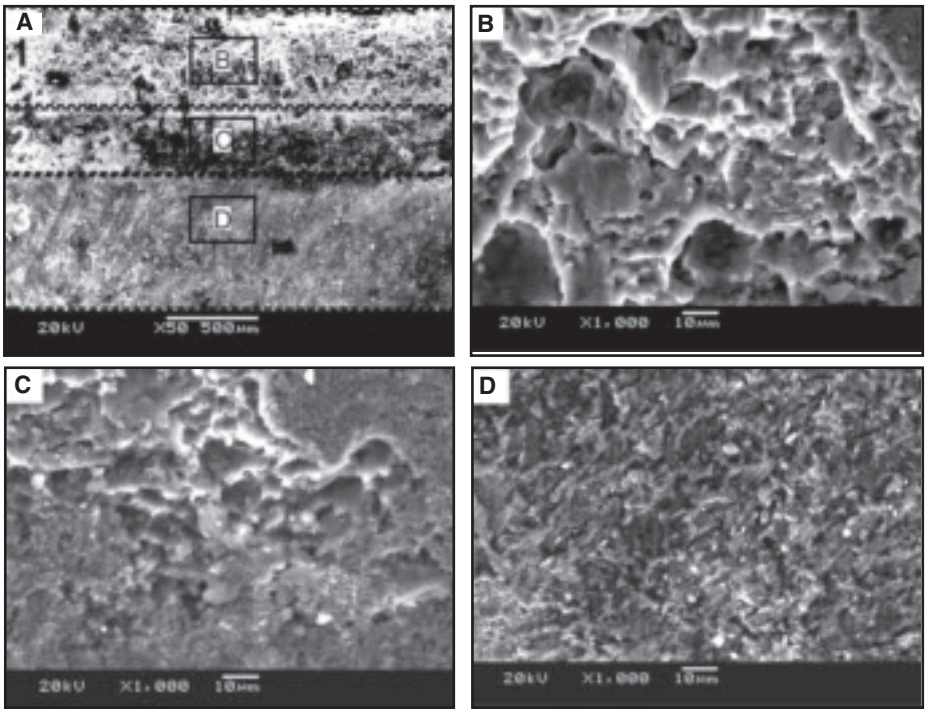

Fig. 13 — SEM images of typical fracture surface of fusion zone side after tensile shear test. A — Fusion zone side including the following: B — top of the surface indicated by B; C — middle of the surface indicated by C; D— bottom of the surface indicated by D.

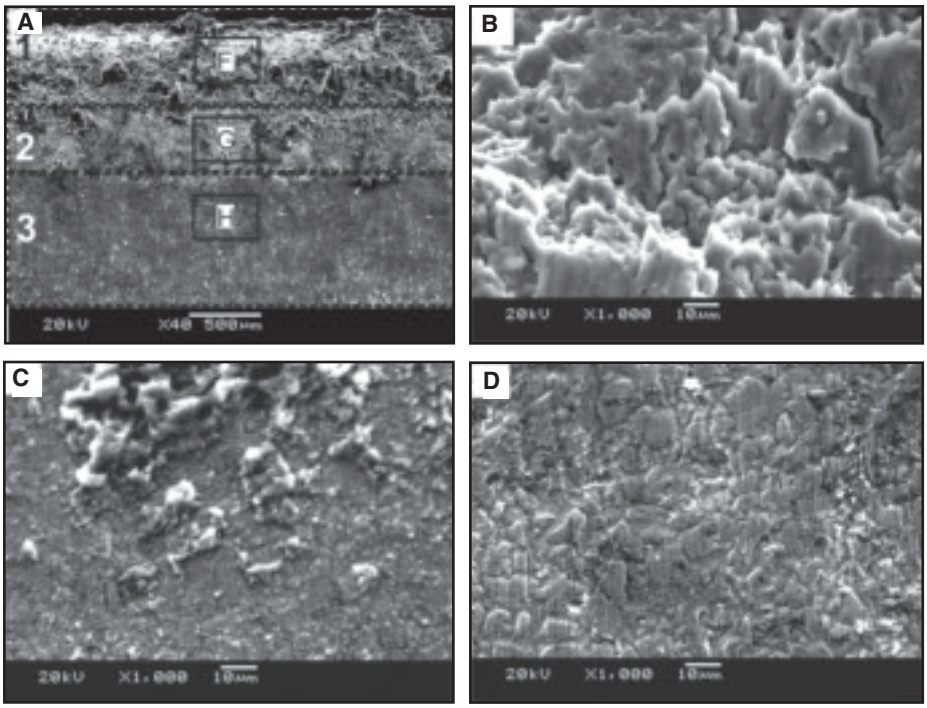

Fig. 14 — SEM images of typical fracture surface of steel side after tensile shear test. A — Steel side including; B — top of the surface indicated by F; C — middle of the surface indicated by G; D — bottom of the surface indicated by H.

of Al, Mg, and Fe across the interface between the fusion zone and steel are shown in Fig. 10. Fe and Al atoms diffused into the fusion zone as a result of high temperature experienced during the laser brazing process. As a result, a diffusion or transition layer formed in front of the IMC layer on the fusion zone side (Refs. 21, 22). According to element distributions of Fe, Al, and Mg (Fig. 10B), in the diffusion layer I with the thickness of almost 1.5 μm, from the FZ side to IMC side, Fe and Al contents increased gradually while the Mg content decreased rapidly. As shown in

Fig. 10A, diffusion layer I is part of the IMC, thus the formation of this diffusion layer led to growth of the IMC layer from 5 to 6.5 μm. The latter occurred at the bottom of the brazed joint. The main mechanism that controls the composition of this area is the time- and temperature-dependent diffusion process.

Another diffusion layer (diffusion layer II) is shown in Fig. 10A on the steel side of the IMC layer between the fusion zone and the steel. The thickness of this layer was ≅3 μm and thus was wider than the diffusion layer I. In this layer, solid-state diffusion is believed to control the overall thickness. During diffusion of an element, the composition gradient is the driving force that allows an element to diffuse to a place of lower concentration. As a result, for diffusion layer I, the elements Fe and Al diffused from the IMC layer to the FZ, but the diffusion direction for the Mg would be the opposite. In diffusion layer II, the IMC layer showed a higher concentration of Al and Mg as compared to steel. Consequently, the diffusion direction changed from the IMC layer to the steel side (for Al and Mg), but Fe atoms diffused into solid solution of the IMC layer (from the steel side). The same type of diffusion layer has been observed by Miao et al. (Refs. 21, 22) after laser penetration brazing of Mg alloy to steel dissimilar joints.

It is worth noting that melting of the Al-12Si coating layer during the laser brazing process not only promoted the growth of the IMC layer in the bottom portion of the interface, but also caused formation and growth of Al/Mg eutectic in the form of β-$Mg_{17}Al_{12}$ phase. Regional quantitative analysis of the chemical compositions by EDS (Table 4) from the middle part of the fusion zone and also near the steel/FZ interface showed that the area near the interface contained 15.7 wt-% Al, which is more than the 11.4 wt-% Al in the middle part of the FZ. This difference is the result of the coarse β-$Mg_{17}Al_{12}$ phase near the interface as compared to the middle part of the FZ.

Mechanical Properties

A Vickers microhardness profile across a brazed joint was measured using 50 g load and 10 s holding time. The microhardness distribution profile is shown in Fig. 11. The average hardnesses of the AZ31B Mg alloy and steel were 62.4 ± 2.3 HVN and 116.3 ± 3.4 HVN, respectively. In the fusion zone, the average hardness increased to 85.7 ± 8.5 HVN due to the strengthening effect of the increased Al content and β-$Mg_{17}Al_{12}$ phase particles in the intergranular regions. The size of the microhardness indenter was too large to measure the hardness of the thin IMC layers formed at the interface. However, higher hardness values are expected for the IMC layer, since the reported average hardness of the θ-$FeAl_3$ phase is 700–800 HVN (Ref. 37), which is much higher than the hardness of the base metals.

Four 50-mm-long × 5-mm-wide tensile specimens were cut out of each sample and tested at a tensile crosshead speed of 1 mm/min. A schematic of the tensile shear test specimen is shown in Fig. 2B. Due to the nonsymmetric configuration of the tensile test specimen, a combination of shear and tensile forces existed at the interface. Consequently, the joint strengths were reported as fracture load, since it is impossible to separate tensile and shear stresses.

The average tensile shear strength of the laser brazed AZ31B-steel joints using Mg-Al filler metal was 767 ± 138 N; representing a 72 ± 13% joint efficiency with respect to the fracture load of the Al-12Si coated steel (1068 N) for the same size tensile specimen. The joint efficiency values were obtained by dividing the fracture load of each laser brazed specimen by the fracture load of the base metal (Al-12Si coated steel). High standard deviation of the tensile shear strength in this study indicates that this laser brazing process for Al-12Si coated steel-AZ31B joints has inherent instability. This instability caused variation in the brazed depth (defined in Fig. 3B) at different locations along the weld interface, which is associated with changing the actual load-carrying area of the joint resulting in different tensile shear strength along the weld interface. Further study is needed to improve the process stability for this dissimilar metal combination.

All tensile shear specimens fractured at the FZ-steel interface. The macro- and microstructure profiles of the joint after fracture are shown in Fig. 12. In each case, fracture initiated in the IMC layer at the bottom of the joint where the geometry of the joint created a high stress concentration area and the thickness of the brittle IMC layer was also at a maximum. Then the crack continued into the brazed FZ at the upper portion of the joint where the IMC layer was thinner. The thick layer of brittle intermetallic at the FZ/steel interface can significantly reduce the strength of the joint as any crack initiating in the layer can easily propagate through this continuous sheet of brittle material (Ref. 38). From these observations, the type and thickness of the IMC layer determined the joint strength. At the bottom of the joint, the thickness of the IMC layer was more than 8 μm, which significantly degraded the mechanical strength of the joints. At the upper portion of the joint, the crack deviated into the FZ and propagated along the grain boundaries of the brazed metal due to existence of β-$Mg_{17}Al_{12}$ phase in the grain boundaries. Therefore, the tensile shear properties and the thickness of the IMC layer appeared to dictate the overall strength of the joints.

Figures 13 and 14 show SEM images of typical fracture surfaces of the fusion zone and steel sides after tensile shear testing, respectively. The fracture morphologies indicate mixed characteristics of brittle and ductile fracture. At the upper portion of the joints (region 1 in Fig. 13A for the FZ side and region 1 in Fig. 14A for the steel side), where the crack propagated into the fusion zone, nonuniform ductile fracture was observed — Figs. 13B and 14B. Meanwhile, at the bottom portion of the fracture surface (regions 3 in Figs. 13A and 14A), where the crack formed in the IMC layer, evidence was seen of more brittle cleavage fracture as shown in Figs. 13D and 14D. In the middle of the fracture surface (regions 2 in Figs. 13A and 14A), an area was observed where the fracture surface contained both ductile and brittle fracture characteristics (see Figs. 13C and 14C). This area is called the transition zone from ductile to brittle fracture modes.

EDS analysis results of the fracture surfaces of both steel and FZ sides are shown in Table 5. At the top of the fracture surface (region B in Fig. 13A for the FZ side and region F in Fig. 14A for the steel side), the composition was similar to the FZ. This implied that the crack propagated into the FZ in the upper portion of the joint. In contrast, at the bottom area of the fracture surface (regions D in Fig. 13A and H in Fig. 14A), the compositions corresponded to the Fe-Al IMC layer indicating that the crack in this region propagated along the IMC layer adjacent to the steel.

Conclusions

Brazed joints between AZ31B-H24 Mg alloy and Al-12Si coated steel have been made by a laser brazing process using a Mg-Al based welding wire in a single flare bevel lap joint configuration. The major conclusions of this study can be summarized as follows:

1. A uniform brazed area with good wetting of base metals was obtained between the AZ31B and Al-Si coated steel sheets using optimized laser brazing parameters. The optimum parameters were 2.2-kW laser power, 8-mm/s travel speed, 0.2-mm beam offset to the steel side using He shielding gas with a flow rate of 30 L/min.

2. A θ-$Fe(Al,Si)_3$ IMC layer was found in the interface between the steel and its Al-12Si coating layer before brazing. During brazing, the high temperature of the process caused this IMC in contact with the coating layer to grow in the form of compact plate-like θ-$Fe(Al,Si)_3$ on the

steel side and needle-like τ_5-$Al_{7.2}Fe_{1.8}Si$ phase on the coating layer side.

3. All of the Al-12Si coating layer was melted and was taken into solution by the molten brazing alloy, thereby promoting good wetting by the Mg-Al filler metal. However, a nonuniform thickness θ-$FeAl_3$ IMC layer was observed at the steel/braze interface after the process. Formation of this layer confirmed the ocurrence of metallurgical bonding between the steel and Mg alloy.

4. The average tensile shear strength of the laser brazed AZ31B-steel joints using Mg-Al filler metal was 767 ± 138 N (72 ± 13% joint efficiency relative to the steel sheet), which strongly depended on the brazed depth of the tensile specimen. Tensile specimens with longer brazed depth, showed higher strength. Cracks formed in the thick IMC layer at the bottom of the joints where there was a stress concentration due to the joint geometry. Cracking then moved into the FZ at the upper part of the joint where the IMC layer was thinner or nonexistent.

Acknowledgments

The authors gratefully appreciate support of the American Welding Society (AWS) Graduate Fellowship Program, the Natural Sciences and Engineering Research Council of Canada (NSERC), and Magnesium Network of Canada (MagNET) for sponsoring this work. The authors would like to acknowledge the comments of Dr. Scott Lawson from the Centre for Advanced Materials Joining at the University of Waterloo.

References

1. Faller, K., and Froes, F. H. 2001. The use of titanium in family automobiles: Current trends. *JOM* 53(4): 27.

2. Rendigs, K. H. 1997. Aluminum structures used in aerospace status and prospect. *Materials Science Forum* 242: 11–24.

3. Wagner, F., Zerner, I., Kreimeyer, M., Seefeld, T., and Sepold, G. 2001. Characterization and properties of dissimilar metal combinations of Fe/Al and Ti/Al-sheet materials. *Proc. ICALEO'01 (CD-ROM)*, Jacksonville, Fla., October. Laser Institute of America: Orlando, Fla.

4. Luo, J. G., and Acoff, V. L. 2000. Interfacial reactions of titanium and aluminum during diffusion welding. *Welding Journal* 79(9): 239-s to 243-s.

5. Kim, Y. C., and Fuji, A. 2002. Factors dominating joint characteristics in Ti-Al friction welds. *Science and Technology of Welding and Joining* 7(3): 149–154.

6. Rodriguez, L., Mathieu, A., Langlade, C., and Vannes, A. 2006. Controlling phase formation during aluminium/steel Nd:YAG laser brazing. *Revista de Metalurgia* 42(6): 463–469.

7. Borrisutthekul, R., Yachi, T., Miyashita, Y., and Mutohc, Y. 2007. Suppression of intermetallic reaction layer formation by controlling heat flow in dissimilar joining of steel and aluminum alloy. *Materials Science and Engineering A* 467: 108–113.

8. Peyre, P., Sierra, G., Deschaux-Beaume, F., Stuart, D., and Fras, G. 2007. Generation of aluminium-steel joints with laser-induced reactive wetting. *Materials Science and Engineering A* 444: 327–338.

9. Mathieu, A., Matte, S., Deschamps, A., Martin, B., and Grevey, D. 2006. Temperature control in laser brazing of a steel/aluminium assembly using thermographic measurements. *NDT and E International* 39: 272–276.

10. Ding, J. J., Huang, H. J., Peyre, P., and Fabbro, R. 2006. Temperature criterion of laser welding for joining aluminum alloy with low-carbon steel. *Materials and Manufacturing Processes* 21: 59–61.

11. Yan, J., Xu, Z., Li, Z., Li, L., and Yang, S. 2005. Microstructure characteristics and performance of dissimilar welds between magnesium alloy and aluminum formed by friction stirring. *Scripta Materialia* 53: 585–589.

12. Chen, Y. C., and Nakata, K. 2009. Effect of tool geometry on microstructure and mechanical properties of friction stir lap welded magnesium alloy and steel. *Materials & Design* 30: 3913–3919.

13. Borrisutthekul, R., Miyashita, Y., and Mutoh, Y. 2005. Dissimilar material laser welding between magnesium alloy AZ31B and aluminum alloy A5052-O. *Science and Technology of Advanced Materials* 6: 199–204.

14. Zhao, X., Song, G., and Liu, L. 2006. Microstructure of dissimilar metal joint with magnesium alloy AZ31B and steel 304 for laser-tungsten inert gas lap welding. *Transactions of China Welding Institution* 27: 1253–1256.

15. Liu, L. M., and Zhao, X. 2008. Study on the weld joint of Mg alloy and steel by laser-GTA hybrid welding. *Materials Characterization* 59: 1279–1284.

16. Qi, X., and Song, G. 2010. Interfacial structure of the joints between magnesium alloy and mild steel with nickel as interlayer by hybrid laser-TIG welding. *Materials & Design* 31: 605–609.

17. Takehiko, W., Kazuhiko, K., and Ronbunshul, Y. G. 2006. Solid state welding of steel and magnesium alloy using a rotating pin. *Quarterly Journal of the Japan Welding Society*, pp. 108–115.

18. Mao, H. K., and Bell, P. M. 1979. Equations of state of MgO and Fe under static pressure conditions. *Journal of Geophysical Research*, pp. 4533–4536.

19. Sierra, G., Peyre, P., Deschaux Beaume, F., Stuart, D., and Fras, G. 2008. Steel to aluminium braze welding by laser process with Al-12Si filler wire. *Science and Technology of Welding and Joining* 13(5): 430–437.

20. Kreimeyer, M., Wagner, F., and Vollertsen, F. 2005. Laser processing of aluminum-titanium-tailored blanks. *Optics and Lasers in Engineering* 43: 1021–1035.

21. Miao, Y., Han, D., Yao, J., and Li, F. 2010. Effect of laser offsets on joint performance of laser penetration brazing for magnesium alloy and steel. *Materials & Design* 31: 3121–3126.

22. Miao, Y., Han, D., Yao, J., and Li, F. 2010. Microstructure and interface characteristics of laser penetration brazed magnesium alloy and steel. *Science and Technology of Welding and Joining* 15(2): 97–103.

23. *ASM Metals Handbook.* 1990. Properties and selection: Nonferrous alloys and special purpose materials. 10th ed. Vol. 2. Materials Park, Ohio: ASM International.

24. Material Safety Data Sheet. 2003. Superior Flux & Mfg. Co. November 11. p. 1.

25. Saida, K., Song, W., and Nishimoto, K. 2005. Diode laser brazing of aluminum alloy to steels with aluminum filler metal. *Science and Technology of Welding and Joining* 10(2): 227–235.

26. Vander Voort, G. F. 1999. *Metallography Principles and Practice.* Materials Park, Ohio. ASM International.

27. Dahle, A. K., Lee, Y. C., Nave, M. D., Schafer, P. L., and StJohn, D. H. 2001. Development of the as-cast microstructure in magnesium-aluminium alloys. *Journal of Light Metals* 1: 61–72.

28. Barbagallo, S., Laukli, H. I., Lohne, O., and Cerri, E. 2004. Divorced eutectic in a HPDC magnesium-aluminum alloy. *Journal of Alloys and Compounds* 378: 226–232.

29. Mathieu, A., Pontevicci, S., Viala, J., Cicala, E., Matte, S., and Grevey, D. 2006. Laser brazing of a steel/aluminium assembly with hot filler wire (88% Al, 12% Si). *Materials Science and Engineering A* 435: 19–28.

30. Li, Y., Ochin, P., Quivy, A., Telolahy, P., and Legendre, B. 2000. Enthalpy of formation of Al-Fe-Si alloys (τ_5, τ_{10}, τ_6, τ_9). *Journal of Alloys and Compounds* 298: 198–202.

31. Maitra, T., and Gupta, S. P. 2003. Intermetallic compound formation in Fe-Al-Si ternary system: Part II. *Materials Characterization* 49: 293–311.

32. Li, Y., and Legendre, B. 2000. Enthalpy of formation of Al-Fe-Si alloys II (τ_6, τ_2, τ_3, τ_8, τ_4). *Journal of Alloys and Compounds* 302: 187–191.

33. Chang, Y. Y., Cheng, W. J., and Wang, C. J. 2009. Growth and surface morphology of hot-dip Al-Si on 9Cr-1Mo steel. *Materials Characterization* 60: 144–159.

34. Bouche, K., Barbier, F., and Coulet, A. 1998. Intermetallic compound layer growth between solid iron and molten aluminium. *Materials Science and Engineering A* 249: 167–175.

35. Viala, J. C., Peronnet, M., Barbeau, F., Bosselet, F., and Bouix, J. 2002. Interface chemistry in aluminium alloy castings reinforced with iron base inserts. *Composites Part A* 33: 1417–1420.

36. Roulin, M., Luster, J. W., Karadeniz, G., and Mortensen, A. 1999. Strength and structure of furnace-brazed joints between aluminum and stainless steel. *Welding Journal* 78(5): 151-s to 155-s.

37. Lin, S. B., Song, J. L., Yang, C. L., Fan, C. L., and Zhang, D. W. 2010. Brazability of dissimilar metals tungsten inert gas butt welding-brazing between aluminum alloy and stainless steel with Al-Cu filler metal. *Materials & Design* 31: 2637–2642.

38. Rathod, M. J., and Kutsuna, M. 2004. Joining of aluminum alloy 5052 and low-carbon steel by laser roll welding. *Welding Journal* 93(1): 16-s to 26-s.